Dynamic modeling of a curling HASEL actuator using the port Hamiltonian framework with experimental validation

Nelson Cisneros[a], Yongxin Wu[a], Kanty Rabenorosoa[a], Yann Le Gorrec[a]

[a] *Université Marie et Louis Pasteur, SUPMICROTECH, CNRS, institute FEMTO-ST, F-25000, Besançon, France*

Abstract

This paper addresses the modeling, parameter identification, and validation of curling Hydraulically Amplified Self-healing Electrostatic (HASEL) actuators using the port Hamiltonian (PH) framework. Employing a modular approach, the HASEL actuator is conceptualized as a combination of elementary subsystems. Each subsystem includes electrical and mechanical components. The electrical component is characterized by a variable capacitor in parallel with a resistor branch, which is in series with another capacitor that is also in parallel with a resistor branch, representing charge retention-related drift. The mechanical component consists of linear and torsional springs connected to an equivalent mass. The parameters of the proposed model were identified using the Levenberg-Marquardt optimization algorithm with data from the developed experimental setup. Additional sets of experimental data were used to validate the obtained model.

Keywords: HASEL actuator, soft actuator, Nonlinear system modeling, Port-Hamiltonian system

---

1. Introduction

In recent years, soft robotics has garnered significant importance, driven by the need for robotic systems that are capable of adapting to diverse environmental conditions. Current designs are often bio-inspired, whereas rigid robots consisting of mechanical systems do not replicate the behavior of natural organisms in the same manner as soft robots. Soft robots can achieve smooth and complex motions such as snakes, elephant trunks, animal tongs, and worms, and replicate muscular movements.

Recently, one of the most captivating advances in soft robotics is the Hydraulically Amplified Self-healing Electrostatic (HASEL) actuator [1]. HASEL actuators combine the advantages of Dielectric Elastomer Actuators (DEAs) and fluid-driven soft actuators, providing convenient electrical control, excellent electro-mechanical performance, large design flexibility, and various modes of actuation [2]. There are various types of HASEL actuators, each distinguished by their shape and motion, including Peano, planar, elastomeric donut, quadrant donut, high-strain Peano, and curling actuators. The literature has documented diverse applications of HASEL actuators, such as a soft gripper for aerial object manipulation [3], an actuator powering a robotic arm [1], an electro-hydraulic rolling soft wheel [4], a Peano actuator for enhanced strain, load, and rotary motion [5], and spider-inspired electrohydraulic soft actuated (SES) joints [6].

The design dimensions have a direct impact on the deformation and torque that can be achieved. As shown in [6], the torque output of SES joints was measured as a function of the hinge angle. In [6] the actuator was tested with various dimensions, including the height, width, and height of the region not covered by electrodes. Two types of films were used: 18 μm thick biaxially oriented polypropylene (BOPP) and 20 μm thick polyester film (brand name L0WS®). At the end a comparison between a servomotor and a SES HASEL was proposed. The servomotor achieved a peak torque of approximately 40 mNm at 5 V, while the SES joint reached a peak torque of approximately 30 mNm. The power consumption of both actuators was also compared throughout an identical series of motions. The servomotor consumed 140 mW while holding the load at 25°, whereas the SES joint consumed less than 1 mW, demonstrating the energetic efficiency of the HASEL actuator.

One significant advantage of HASEL actuators is the use of dielectric fluids, which enhances their reliability and scalability, improving their ability to self-repair after dielectric breakdown. Additionally, HASEL actuators can achieve higher deformation levels than DEAs due to their design allows broader and more flexible movements [1]. HASEL actuators are highly versatile and capable of achieving expansion, contraction, and rotation. They can self-sense their deformation state and be constructed from various material systems with multiple form factors and sizes. Current HASEL actuator designs exhibit muscle-like performance, making them a viable alternative to other types of artificial muscles. Furthermore, HASEL artificial muscles represent a nascent field of research with significant potential for enhanced performance [2]. The main challenges associated with HASEL actuators include the need for high operating voltage, the importance of preventing dielectric liquid leakage in case of pouch damage, and the difficulty in maintaining a constant position under a steady voltage. The authors of [7] characterize an individual HASEL bending actuator, or 'finger', demonstrating controllable pinch force up to 0.7 N, repeatable capacitance

---

Email addresses: `nelson.cisneros@femto-st.fr` (Nelson Cisneros), `yongxin.wu@femto-st.fr` (Yongxin Wu), `rkanty@femto-st.fr` (Kanty Rabenorosoa), `yann.le.gorrec@ens2m.fr` (Yann Le Gorrec)

change to displacement, and fast tunable grip speeds (as low as 50 ms to grip). They feature different gripper configurations capable of grasping a wide variety of objects, including delicate fruits.

Adding a strain limiting layer introduces anisotropic behavior; bending occurs on the opposite side of the layer, enabling the transition from a linear to an angular deformation mechanism [2]. Curling HASEL actuators can be used to manufacture more complex actuators thanks to their versatility, durability, and ability to mimic natural movements. Establishing a reliable model to accurately represent system dynamics is crucial for achieving effective actuator control in the next step.

Recently, various models have been proposed to represent the behavior of HASEL actuators under different assumptions. [8] employs a hyperelastic neo-Hookean model to characterize the coupled elastic-electrical-hydraulic behavior of a donut-shaped HASEL actuator within the quasi-static domain. The authors of [9] and [10] used the free energy of the system to derive analytical models representing the quasi-static response of a Peano-HASEL actuator and a high-strain Peano-HASEL actuator, respectively. The authors of [11] propose a dynamic model of a peano-HASEL actuator based on dimensional analysis and Lagrange's second-order law. In [12], Dynamic Mode Decomposition with control (DMDc) leads to a linear model that approximates the system dynamics. The authors of [13] proposed a nonlinear reduced-order mass spring damper (MSD) approximation of an assembly of HASEL actuators. The authors of [14] studied the film material deformation, dielectric liquid dynamics, and actuator electrical conditions. They used finite element analysis with COMSOL Multiphysics software to develop a generalized physics-based framework representing the actuation mechanism. Data-driven models are used to model and control soft actuators [15], yielding good results. However, the main limitation of such models is that they are typically black-box representations, offering limited insight into the underlying physical phenomena.

The referenced articles offer various methodologies for modeling HASEL actuators; however, none is well suited for the dynamic modeling of curling HASEL actuators. The model presented by [16] has focused on the Peano-type HASEL actuator, which exhibits simple vertical contraction, with all actuator units (each pouch) moving in the same direction. As a result, the underlying model relied on strong assumptions, making its geometrical modeling relatively straightforward. Furthermore, this work did not account for the drift effect and the response to an AC input signal is not addressed in this model. Hence, drawing on the concepts outlined in [16], taking advantage of the port-Hamiltonian (PH) approach, we introduce new multiphysics elements to establish a representative model of the complex dynamic behavior of a HASEL actuator across its electrical and mechanical domains while addressing their coupling through the principles of volume conservation. In addition, we included the drift effect induced by charge retention in the actuator materials in the model representation. The proposed model is well-suited for control purposes. Taking advantage of the port-Hamiltonian framework, passivity-based control methods, such as the Interconnection and Damping Assignment Passivity-Based Control (IDA-PBC) method, can be applied to achieve target positions or generate desired forces, as required in gripper applications. An example of passivity-based control applied to a soft planar vertical take-off and landing (Soft-PVTOL) aircraft is presented in [17].

To address the flexibility and large deformations of the curling HASEL actuator, this work adopts a finite-dimensional model based on nonlinear ordinary differential equations. Although infinite-dimensional models using partial differential equations (PDEs) offer high accuracy, their complexity and computational demands, particularly under nonlinear deformations, make them impractical for real-time control. The proposed lumped-parameter nonlinear model provides a practical approximation of the system dynamics and enables efficient implementation of passivity-based controllers.

The main contributions of this paper are as follows:

- Modeling of a curling HASEL actuator using the PH approach to capture electrical and mechanical behaviors of the actuator. The drift effect is accounted for by adding a resistor branch parallel to the capacitor that represents the electrodes, both in series with a capacitor that is also in parallel with a resistor branch that represents charge retention. Volume conservation allows coupling of the electric and mechanical domains.
- The derivation of a complex system from the interconnection of several basic elements takes advantage of the modularity principle in the PH framework.
- Identification of key design parameters for curling HASEL actuators. The stiffness K_b, damping b, and input mapping as the cosine of the endpoint position were derived from the experimental data and validated against other experimental conditions.
- The model of a Manta Ray bio-inspired soft robot is presented to demonstrate the applicability of the proposed modeling methodology to other HASEL actuator-based systems.

This paper is organized as follows: Section 2 gives a detailed literature review of existing modeling for HASEL actuator and describes the curling HASEL actuator considered in this work. The dynamic model of the presented curling HASEL actuator is proposed in Section 3 using the PH framework. Then, we show in Section 4 the identification and validation results. Finally, Section 5 gives final remarks and future work.

2. Existing models, curling HASEL actuator description and modeling assumptions

2.1. Existing HASEL actuator models in literature

In this section, we first introduce the existing modeling approaches in the literature. The authors in [8] used a hyperelastic neo Hookean model to characterize the coupled elasto-electrical-hydraulic behavior of a donut-shaped HASEL actuator within the quasi-static domain. In [6] a quasi-static model of spider-inspired electrohydraulic soft-actuated joints is presented. The authors of [9] and [10] use the free energy of the system to derive an analytical model that represent the quasi-static response of a Peano-HASEL and a high strain Peano-HASEL actuator respectively. The authors of [11] show the dynamic model of a Peano-HASEL actuator, based on dimensional analysis and Lagrange's second order law. They derive a timescale that describes the influence of geometry, materials system, and applied external loads on the actuation speed. In [13], the authors introduce a non-linear quasi-static reduced-order mass-spring-damper (MSD) model for a robotic manipulator actuated by six HASELs. They demonstrate that simulations based on the non-linear MSD models effectively anticipate the physical behavior of the robot on a macro scale. In [12], Dynamic Mode Decomposition with control (DMDc) is used to acquire a linear model that approximates the system dynamics of a HASEL arm. The study described in [14] investigates the deformation of film materials, the dynamics of dielectric liquids, and the electrical conditions of the actuator. The authors employ finite element analysis software COMSOL Multiphysics to develop a generalized physics-based framework for representing the actuation mechanism. In [18] an artificial muscle fibre that simulates human triceps surae muscle fibre using Peano-HASEL actuators is represented by a finite element model.[19] presents a model that represents the quasi-static response of Electrostatic Multilayered Systems (EMSs). This approach captures the drift effect and allows its reduction by selecting the materials that constitute the actuators. The approach is used in a Peano-HASEL actuator. Kellaris et al. (2021) presents a quasi-static model to represent the behavior of soft-actuated electrohydraulic joints. In [16], a Port-Hamiltonian (PH) formulation of a one-degree-of-freedom (DOF) HASEL planar actuator is introduced. A nonlinear spring-damper system is used to approximate the mechanical deformation of the actuator resulting from fluid motion, while a nonlinear capacitance model is used to approximate the electrical behavior of the system but the drift effect is not considered in this work.

Our work presents a dynamic model of a curling HASEL actuator, whereas [6] provides a quasi-static model of spider-inspired electrohydraulic soft joints. In this work, the model captures the drift effect, which is a characteristic of HASEL actuators, and also represents the current consumption of the actuator, which is not accounted for in the model presented in [16]. This model is based on physical principles, unlike the model presented in [12]. The model presented here is designed for control applications, and its modularity allows it to be adapted for other HASEL actuator configurations. A detailed summary of the existing modeling approaches is presented in Table. 1.

Table 1: HASEL models existing in the literature

Ref.	Model type	HASEL actuator type	Contribution
[6]	Analytical model	Spider-inspired electrohydraulic soft-actuated joints	Quasi-static model No drift effect
[8]	Finite element model	Single donut type actuator	Quasi-static model No drift effect
[9]	Analytical model	Peano	Quasi-static model No drift effect
[10]	Analytical model	HS-Peano	Quasi-static model No drift effect
[11]	Analytical model	Peano	Dynamic model No drift effect and not suitable for control
[12]	Data-driven model-based	Peano	Data-driven model No physical model, not easy to generalize
[13]	Analytical model	Folded individual pouches	Quasi-static model No drift effect
[14]	Finite element model	Individual pouch	Dynamic model No drift effect and not suitable for control
[16]	Analytical model	Peano	Dynamic model PH model describes the dynamics No drift effect
[18]	Finite element model	Peano	Dynamic model No drift effect and not suitable for control
[19]	Analytical model	Peano	Quasi-static model Drift effect and suitable for material selection
Our work	Analytical model	Curling HASEL	Dynamic model with Drift effect Modular approach and Control oriented model

2.2. *Actuator description*

This section describes the curling HASEL actuator and associated experimental setup, as illustrated in Figure 1. The curling HASEL actuator was fabricated using a planar HASEL attached to the strain-limiting layer. The bending motion was obtained by applying high voltage to the electrodes of the actuator. Bending deformation was measured using a profile laser sensor. The curling HASEL actuator is composed of several pouches (sic C-Series Contracting HASEL Actuator, Artimus$^{®}$ Robotics with dimensions $76.2 \times 147 \times 3.4$ *mm*) that contain dielectric liquid (Envirotemp FR3$^{®}$); each pouch is conformed by two films of biaxially oriented polypropylene, which are partially covered by carbon paint electrodes. A schematic representation of the actuator is shown in Figure 2a. The system is partitioned into basic subsystems (Figure 2b). Each basic subsystem comprise electrical and mechanical parts. The experimental setup used a Keyence$^{®}$ LJ-V7080 profile laser sensor to measure the actuator position.

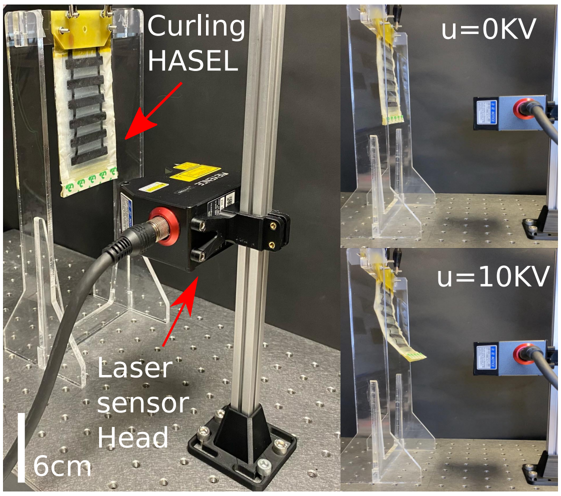

Figure 1: In the left figure the curling HASEL actuator and the laser sensor head used to register the displacement are shown. The right figures show the curling HASEL displacement from the equilibrium position with an input of 0 kV and the actuator deformation when the applied voltage is 10 kV.

2.3. *Assumptions*

We present the assumptions taken into account in modeling the curling actuator. First, the width of the actuator was assumed to be uniform; thus, a two-dimensional analysis was conducted.

Assumption 1. The model is composed of subsystems as described in Figure 2a. Each subsystem is composed of a chamber and a shell, as depicted in Figure 2b. The corresponding notation is presented in Table 2. The chamber is the area between the electrodes, and the shell is the part of the pouch that receives the dielectric liquid when the electrodes are zipped.

Assumption 2. The total volume (the volume of the shell plus the chamber volume) is considered constant and the dielectric liquid is incompressible. The bending of the bottom film was modeled as a torsional spring.

Assumption 3. The top film of the shell is assumed to be extendable and to store mechanical energy. The elongation was modeled as a linear spring. The volume of the liquid dielectric in the chamber is transferred to the shell as a function of the zippered area induced by the applied voltage.

Assumption 4. The material is homogeneous throughout the actuator. Therefore, the parameters to be identified are the same for all subsystems.

Table 2: Notation and definition

Symbol	Units	Definition
R_0^i	Ω	Equivalent resistance
R_1^i	Ω	Equivalent resistance
R_2^i	Ω	Equivalent resistance
C_1^i	F	Capacitance related to drift effect
C_2^i	F	Variable capacitor
K_i	N/m	Linear spring stiffness
K_b^i	Nm/rad	Torsional spring stiffness
X_h	m	Chamber high
m_i	kg	Mass of the actuator
δ_1^i	rad	Auxiliary angle
θ_i	rad	Angular position
l_e^i	m	Electrodes zipped lenght
L_e	m	Electrodes lenght
L_v	m	Length of bottom film
l_p^i	m	Length of top film
A_s^i	m^2	Area of the shell

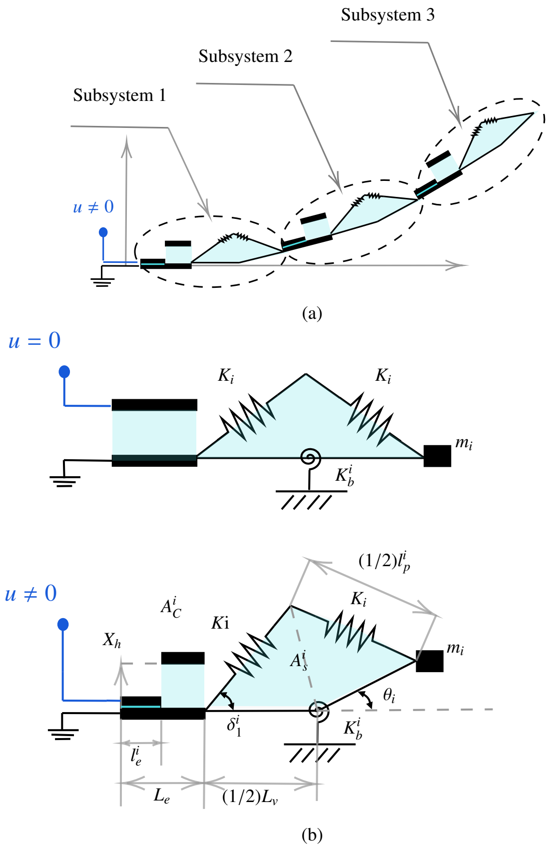

Figure 2: 2a) illustrates the cross-section of the Curling HASEL actuator, where the subsystems are interconnected to represent the entire actuator. The same voltage is applied to each subsystem. 2b) the basic subsystem is illustrated. On the left, the electrodes are fully unzipped, while on the right, the electrodes are partially zipped when voltage is applied, resulting in shell deformation.

2.4. Geometric relations

This section discusses for each subsystem i the geometric relations that link the deformation angle θ_i with the zipped electrode length l_e^i. Therefore, from θ_i, one can derive the actuator endpoint position $h(\theta)$, that is, the displacement of the actuator tip position. Establishing a relationship between θ_i and l_e^i is crucial, because the capacitance of the the electrode can be expressed as a function of l_e^i. This relation enables us to connect the electrical charge with the derivative of the electrical energy with respect to the angle θ_i, thereby coupling the electrical and mechanical components of the system.

We assumed that the chamber has a rectangular area, and the shell was modeled as two symmetric triangles. Figure 2b shows the different variables of a basic subsystem. The following equations allow us to determine the relationship between the θ_i angle and zipped electrode length l_e^i. The area inside a single shell A_s^i can be computed as:

$$A_s^i = \frac{1}{4} l_p^i L_v sin(\delta_1^i(\theta_i, l_p^i)) \tag{1}$$

with

$$\delta_1^i(\theta_i, l_p^i) = \frac{\pi + \theta_i}{2} - \sin^{-1}\left(\frac{L_v}{l_p^i}\sin\left(\frac{\pi - \theta_i}{2}\right)\right), \tag{2}$$

where $i \in \mathbb{N}$ denotes the index of an individual subsystem. The constant L_v is the shell bottom length. The total area (area of the chamber + area of the shell) A_T is constant because we assume that the dielectric liquid is incompressible. It can be computed from its initial position when the electrodes are unzipped ($l_e^i = 0$), as shown in Figure 2b. Furthermore, the total area can be related to the zipped length of the electrode l_e^i of each subsystem using the following equation:

$$A_T = A_s^i + X_{h_i}(L_e - l_e^i(\theta_i, l_p^i)), \tag{3}$$

where X_h is the height of the chamber, and L_e is the length of the chamber. The total area A_T is equal to the sum of the unzipped areas of the shell and chamber.

The zipped electrode length depends on the angle $\delta_1^i(\theta_i, l_p^i)$ which is a function of the top film length l_p^i and angular position θ_i:

$$l_e^i(\theta_i, l_p^i) = L_e - \frac{1}{X_h}\left(A_T - \frac{L_v l_p^i}{4} sin(\delta_1^i(\theta_i, l_p^i))\right). \tag{4}$$

The endpoint displacement of the HASEL actuator with $n \in \mathbb{N}$ interconnected subsystems can be computed as

$$h(\theta) = (L_v + L_e)\left(\sum_{j=1}^{n} \sin\left(\sum_{i=1}^{j} \theta_i\right)\right). \tag{5}$$

Remark 1. A dynamic model comprising four elements adequately captures the observed dynamical behavior in the experimental measurements. This number of elements strikes a balance between capturing the essential dynamics of the system and maintaining the computational efficiency. Although a higher number of elements could potentially improve the precision of the model, it would also increase its computational complexity and resource requirements.

2.5. Electric subsystem and charge retention

This subsection deals with the electric behavior of the actuator, focusing on the drift effect observed during the experiment. The drift effect, attributed to the charge retention phenomenon as documented in the literature [20], manifests itself as a position drift when a constant voltage is applied to the actuator. The applied electric field induces Maxwell stress, which zips the electrodes. However, charge retention within the actuator generates an internal electric field opposite to the external electric field, leading to the observed drift effect (see Figure 3).

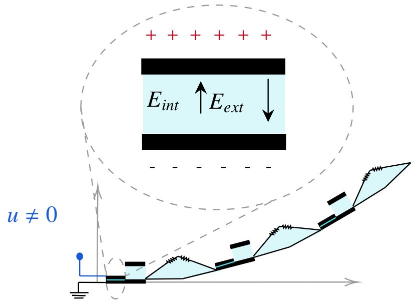

Figure 3: Charge retention phenomenon. The wrapped internal electric field inside the pouch is opposite the external electric field, decreasing the Maxwell stress over time.

R_1^i denotes the resistance of the electrodes. The series circuit of capacitor C_1^i and resistance R_2^i represents charge retention. Capacitor C_2^i presents the dynamics of parallel electrodes of the HASEL actuator. Capacitor C_2^i has two parts whose capacitance depends on the zipped and unzipped areas (see Figure 4).

3. Curling HASEL port-Hamiltonian model

In this section, we model curling HASEL actuator dynamics using the PH framework. First, let us briefly recall the PH model in [21].

$$\begin{aligned} \dot{x} &= [J(x) - R(x)]\nabla_x H(x) + g(x)u; \\ y &= g^\top(x)\nabla_x H(x)(x), \end{aligned} \tag{6}$$

where $x \in \mathbb{R}^n$, $J(x) = -J^\top(x)$ is the interconnection matrix, $R(x) = R^\top(x) \geq 0$ is the dissipation matrix and $H(x)$ is the total energy of the system.

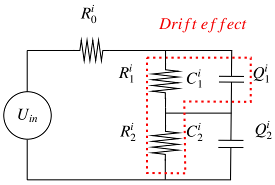

Figure 4: An equivalent electrical circuit is proposed, consisting of a resistor R_0^i that represents the resistance in the connectors, the resistance R_1^i in parallel with a capacitor C_1^i that represents the material charge retention in series with a dynamic capacitor C_2^i, in parallel with resistance R_2^i. This configuration accounts for the drift effect arising from material charge retention.

The model consists of the following parts:

- The interconnection J and dissipation matrix R, which relates the energy exchanges between the sub components and the energy dissipation in the system.
- The vector of co-energy variables, $\nabla_x H(x)$, which is defined as the gradient of the Hamiltonian $H(x)$ with respect to the states x.
- The input map, defined as $g(x)$, and the input u.
- The output, which is the power-conjugated variable of the input. For this model, it corresponds to the system's current.

The modeling methodology is shown in Figure 5.

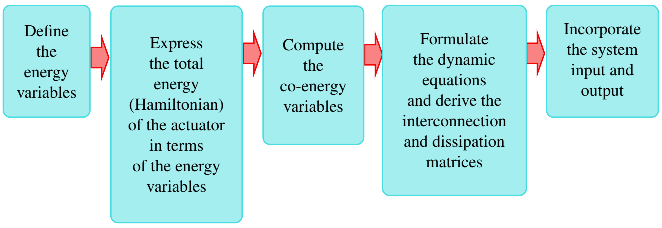

Figure 5: Methodology for formulating the PHS model.

By combining the basic subsystems in a power preserving manner, that is equaling velocities and forces, we can represent the overall dynamic behavior of the HASEL actuator, as shown in Figure 6. Analogous to a two-degree-of-freedom manipulator, a_c^i represents the distance between the joint and the center of mass of the link and a_i denotes the link length. The mass is denoted as m_i.

We define the energy variables as the state variables

$$x = \left[\theta^\top,\ l_p^\top,\ p^\top,\ Q_1^\top,\ Q_2^\top\right]^\top \tag{7}$$

where θ is the torsional spring angular position vector, l_p is the top film length vector, p is the momentum of the tip mass vector, Q_1 and Q_2 are the electrical charges vectors of the capacitors C_1 and C_2, respectively. With these energy variables, the total energy of the actuator (Hamiltonian) is composed of the

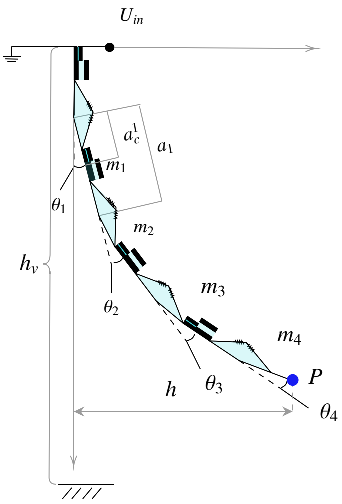

Figure 6: The interconnection of subsystems represents the entire behavior of the system.

following five components:

$$H(\theta, l_p, p, Q_1, Q_2) = \underbrace{H_\theta(\theta)}_{\text{Torsional spring}} + \underbrace{H_{l_p}(l_p)}_{\text{Linear spring}} + \underbrace{H_g(\theta)}_{\text{Gravity}} + \underbrace{H_p(p)}_{\text{Kinetic}} + \underbrace{H_Q(Q_1, Q_2, \theta, l_p)}_{\text{Electrical}}. \tag{8}$$

The first term in (8) is the potential energy related to the torsional spring:

$$H_\theta = \frac{1}{2}\sum_{i=1}^{n} K_b^i \theta_i^2 = \frac{1}{2}\theta^\top K_b \theta \tag{9}$$

where $K_b = \mathrm{diag}[K_b^1\ K_b^2\ \ldots\ K_b^n]$ is the stiffness matrix and $\theta = [\theta_1\ \theta_2\ \ldots\ \theta_n]^\top$ represents the angular vector of each subsystem.

The second term in (8) is the potential energy related to the top film elongation, which reads:

$$H_{l_p} = \frac{1}{2}\sum_{i=1}^{n} K_i (l_p^i - L_p)^2 = \frac{1}{2}(l_p - L_p)^\top K (l_p - L_p), \tag{10}$$

where $K = \mathrm{diag}[K_1\ K_2\ \ldots\ K_n]$ and $l_p = [l_p^1\ l_p^2\ \ldots\ l_p^n]^\top$.

The third term of the energy in (8) is the potential energy related to gravity. Each subsystem can be considered as a link interconnected in series with the other subsystems. The potential energy associated with gravity is given by:

$$H_g = \sum_{i=1}^{n} m_i \bar{g}\left(h_v - \left(a_{c_i}\cos\left(\sum_{j=1}^{i}\theta_j\right) + \left(\sum_{j=1}^{i-1} a_j \cos\left(\sum_{k=1}^{j}\theta_k\right)\right)\right)\right);$$

where $\bar{g}$ is the gravitational acceleration constant, and h_v is the actuator height.

The kinetic energy (fourth term of (8)) is then given by:

$$H_p = \frac{1}{2}p^\top M^{-1} p. \tag{11}$$

M is the inertia matrix and p is the vector of angular momenta $p = [p_1\ p_2\ \ldots\ p_n]^\top$.

$$M = \sum_{i=1}^{n}(m_i J_v^{i\,\top} J_v^i + J_w^{i\,\top} \tilde{I}_i J_w^i) \tag{12}$$

where J_v^i and J_w^i are the *ith* linear and angular velocities Jacobians and $\tilde{I}_i = (1/12)a_i m_i$ is the inertia.

The last term of (8) is the electrical energy stored in the capacitors, which can be represented as:

$$H_Q = \frac{1}{2}\sum_{i=1}^{n}\left(\frac{(Q_1^i)^2}{C_1^i} + \frac{(Q_2^i)^2}{C_2^i}\right) = \frac{1}{2}Q_1^\top C_1^{-1} Q_1 + \frac{1}{2}Q_2^\top C_2^{-1} Q_2, \tag{13}$$

where $C_1 = \mathrm{diag}[C_1^1\ C_1^2\ \ldots\ C_1^n]$ is the constant capacitance that represents the charge retention effect of the actuator. $C_2 = \mathrm{diag}[C_2^1\ C_2^2\ \ldots\ C_2^n]$ is the dynamic capacitance that represents the electrodes, films, and dielectric liquid, computed as the sum of the capacitance of the zipped electrodes and the capacitance of the unzipped electrodes.

$$C_2^i(\theta_i, l_p^i) = \epsilon_0 \epsilon_r w\left(\frac{l_e^i(\theta_i, l_p^i)}{2t} + \frac{L_e - l_e^i(\theta_i, l_p^i)}{2t + X_h}\right) \tag{14}$$

where ϵ_0 is the vacuum permittivity, ϵ_r is the relative permittivity, w is the actuator width, t is the film thickness, L_e is the chamber length and l_e^i is the length of the zipped electrodes part. X_h is the chamber height. $Q_1 = [Q_1^1\ Q_1^2\ \ldots\ Q_1^n]^\top$ and $Q_2 = [Q_2^1\ Q_2^2\ \ldots\ Q_2^n]^\top$ are the electric charges.

Once the state (energy) variables and Hamiltonian of the system are defined, we introduce the dynamics of the actuator. First, the angular velocity of a single subsystem is equal to:

$$\dot{\theta}_i = \frac{\partial H_i}{\partial p_i} = \frac{p_i}{\tilde{I}_i} \tag{15}$$

The time variation of the top film length is $\dot{l}_p^i = v_m^i \sin(\delta_1^i)$, where v_m^i is the mass velocity defined as $v_m^i = \frac{L_v}{2}\dot{\theta}_i$. From the definition of A_s^i, we derive the expression for $\sin(\delta_1^i) = \frac{A_s^i}{l_p^i}\frac{4}{L_v}$. Thus, the time variation of the top film is given as:

$$\dot{l}_p^i = \frac{2A_s^i}{l_p^i}\frac{\partial H}{\partial p_i}. \tag{16}$$

Therefore, the relation between the time derivative of the top film length $\dot{l}_p^i$ and the partial derivative of the Hamiltonian with respect to the angular momentum of a single subsystem is given by the term $\frac{2A_s^i}{l_p^i}$.

The angular momentum variation of a single subsystem with respect to time is:

$$\dot{p}_i = -K_b^i\theta_i - \frac{L_v}{2}m_i\bar{g}\sin(\theta_i) - \frac{\partial H_{Q_2}^i}{\partial \theta_i} - \frac{A_s^i K_i (l_p^i - L_p)}{l_p^i} - \frac{2A_s^i}{l_p^i}\frac{\partial H_{Q_2}^i}{\partial l_p^i} - b_i\frac{p_i}{\tilde{I}_i}. \tag{17}$$

Thus, we can write the equation for n interconnected subsystems as:

$$\dot{p} = -\frac{\partial H}{\partial \theta} - d\frac{\partial H}{\partial l_p} - b\frac{\partial H}{\partial p} \tag{18}$$

where $b = \mathrm{diag}[b_1\ b_2\ ...\ b_n]$ and $d = \mathrm{diag}[\frac{2A_s^1}{l_p^1}\ \frac{2A_s^2}{l_p^2}\ \ldots\ \frac{2A_s^n}{l_p^n}]$.

The charge variation of the two electrical charges Q_1 and Q_2 with respect to time is derived as follows:

$$\dot{Q}_1 = \bar{R}_0 ga U_{in} - \bar{R}_0 C_1^{-1} Q_1 - \bar{R}_1 C_1^{-1} Q_1 - \bar{R}_0 C_2^{-1} Q_2, \tag{19}$$

$$\dot{Q}_2 = \bar{R}_0 ga U_{in} - \bar{R}_0 C_1^{-1} Q_1 - \bar{R}_0 C_2^{-1} Q_2 - \bar{R}_2 C_2^{-1} Q_2, \tag{20}$$

where the inverse value of the equivalent electrical circuit resistances are defined as $\bar{R}_0 = \mathrm{diag}[\frac{1}{R_0^1}\ \frac{1}{R_0^2}\ ...\ \frac{1}{R_0^n}]$,
$\bar{R}_1 = \mathrm{diag}[\frac{1}{R_1^1}\ \frac{1}{R_1^2}\ ...\ \frac{1}{R_1^n}]$ and $\bar{R}_2 = \mathrm{diag}[\frac{1}{R_2^1}\ \frac{1}{R_2^2}\ ...\ \frac{1}{R_2^n}]$. The input mapping is denoted by $ga = [ga_1\ ga_2\ ...\ ga_n]^\top$. To capture the system's nonlinearity in the inputs, we choose a function of the form $ga_i = \gamma_1 \cos(\gamma_2 \theta_i)$ to reflect the observed experimental behavior, where γ_1 and γ_2 are parameters to identify. We observed from the experimental data that the relationship between the response of the actuator and input voltage can be approximated by a cosine function that depends on the angular position.

From (15)–(20) and the expression of the Hamiltonian (8), one can write the PH model of the curling HASEL actuator as :

$$\underbrace{\begin{bmatrix} \dot{\theta} \\ \dot{l}_p \\ \dot{p} \\ \dot{Q}_1 \\ \dot{Q}_2 \end{bmatrix}}_{\dot{x}} = \underbrace{\begin{bmatrix} 0 & 0 & I & 0 & 0 \\ 0 & 0 & d & 0 & 0 \\ -I & -d & -b & 0 & 0 \\ 0 & 0 & 0 & -(\bar{R}_0 + \bar{R}_1) & -\bar{R}_0 \\ 0 & 0 & 0 & -\bar{R}_0 & -(\bar{R}_0 + \bar{R}_2) \end{bmatrix}}_{J-R} \underbrace{\begin{bmatrix} \nabla_\theta H \\ \nabla_{l_p} H \\ \nabla_p H \\ \nabla_{Q_1} H \\ \nabla_{Q_2} H \end{bmatrix}}_{\nabla_x H}$$

$$+ \underbrace{\left[0\ 0\ 0\ \bar{R}_0 ga(\theta)^\top\ \bar{R}_0 ga(\theta)^\top\right]^\top}_{g} U_{in}; \tag{21}$$

$$y = \underbrace{(\bar{R}_0 ga(\theta))^\top C_1^{-1} Q_1 + (\bar{R}_0 ga(\theta))^\top C_2^{-1} Q_2}_{g^\top \nabla_x H}.$$

The output $y = i_e$ is the current, that is the power-conjugated variable to the input voltage. The energy balance equation can be written as:

$$\begin{aligned} \frac{\partial H}{\partial t} &= -\frac{\partial H^T}{\partial x} R \frac{\partial H}{\partial x} + y^\top u; \\ \frac{\partial H}{\partial t} &\leq y^\top u = i_e U_{in}. \end{aligned} \tag{22}$$

The model parameters are shown in Table 3. The relative permittivity parameters are taken from [6].

In summary, the methodology for formulating the model is as follows.

1. Define the energy variables (7) corresponding to the different components of the curling HASEL actuator.
2. Express the total energy (Hamiltonian) of the actuator (8) in terms of the energy variables. The Hamiltonian is defined as the sum of the mechanical potential and kinetic energies, and the electrical energy associated with the electrical subsystem.
3. Compute the co-energy variables by evaluating the gradient of the Hamiltonian with respect to the energy variables, $\nabla_x H$.
4. Formulate the dynamic equations and derive the interconnection and dissipation matrices, which describe the relationship between the energy variables and co-energy variables. It is essential to incorporate the geometric constraints and relations inherent to the system during this process.
5. Incorporate the system input and output. The input of the system (input voltage) is multiplied by the input map. The output of the system is defined as the power conjugate variable associated with the input, which, in this case, corresponds to the current of the system.

Table 3: Model parameters

Symbol	Value	Units	Definition
L_p	0.015	m	Initial length of top film
L_v	0.015	m	Length of bottom film
L_e	0.015	m	Length of electrodes
X_h	0.002	m	Chamber high
m_i	0.007	kg	Mass
ϵ_r	2.2	F/m	Relative permittivity
ϵ_0	8.854x10^{-12}	F/m	Vacuum permittivity
w	0.05	m	Actuator width
t	18×10^{-6}	m	Film thickness

4. Model identification and validation

In this section, we identify the system parameters using experimental data obtained from the setup shown in Figure 1. This experimental setup employed a Keyence® LJ-V7080 profile laser sensor to measure the actuator position. The sensor accuracy is ±0.1% of full scale and the sampling time is 1 ms. The input voltage was supplied by a Trek® 610E high-voltage amplifier controlled by a dSPACE board CLP1104. The current was monitored using a high-voltage amplifier. The actuator used to validate the model was the Artimus® Robotics HASEL C-Series actuator (C-5015-06-01-B-ACAC-50-096), which was attached to a strain-limiting layer (polymer sheet, 76.2 × 120 × 0.08 mm). We used a dSPACE board CLP1104 to receive the measured position signal from the laser position sensor and current from the amplifier. The dSPACE board transmitted the input signals to the high-voltage amplifier. The system identification results comprised four interconnected subsystems that approximated the curling HASEL actuator.

4.1. Identification by Nonlinear grey box

To identify the system parameters, we used a gray box identification method. First, we characterized the most sensitive parameters from the model response. Figure 7 shows the system response to a 5 kV step input. From this response, we can determine the sensitive parameters as follows:

- Damping (b): This parameter was adjusted to regulate the amplitude of the oscillations.
- Torsional spring stiffness (K_b): This parameter was adjusted to regulate the frequency of the oscillations.
- Capacitance (C_1) and conductances ($\bar{R}_1$ and $\bar{R}_2$): These parameters are adjusted to account for the position drift effect.
- Input gain (ga): This parameter is adjusted to correctly scale the input voltage.
- Equivalent electrical circuit conductance ($\bar{R}_0$): This parameter is adjusted to define the electrical behavior of the system.

We can fine-tune the model to accurately reflect the system dynamics across different input voltages by focusing on these parameters. The initial parameter values have been manually tuned by comparing the simulation results with experimental data to achieve an acceptable fit. Using these initial values, the Levenberg-Marquardt optimization algorithm is then used for parameter identification. To determine these initial values, we followed a multistep approach. First, parameters related to the physical properties of the actuator—such as the mass m, the length of top film L_p, the length of electrodes L_e, actuator width, height and film thickness—were obtained through direct measurement from the real actuator. The permittivity for the electrical component was obtained from the literature.

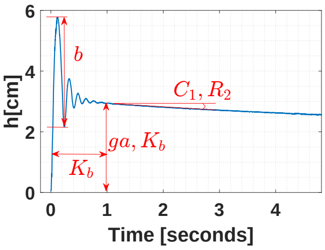

Figure 7: Parameter sensitive and their effect in the dynamics and steady-state behavior.

The identified model parameters are listed in Table 4. Following this, we adjusted the resistance R_0^i to fine-tune the total current peaks of the system.

Table 4: Identified model parameters

Symbol	Value	Units	Definition
R_0^i	1×10^3	Ω	Equivalent resistance
R_1^i	1×10^6	Ω	Equivalent resistance
R_2^i	1.47×10^6	Ω	Equivalent resistance
C_1^i	1.75×10^{-5}	C	Capacitance related to drift effect
K_i	20.83	N/m	Spring constant
K_b^i	0.04	Nm/rad	Torsional spring constant
b_i	0.0031	kgs	Damping
γ_1	40.38	-	Gain parameter
γ_2	7.05	-	Gain parameter

The final step involves model validation, where we compare the model response with the experimental data to ensure accuracy and reliability.

Figure 8 shows the identification results obtained using a negative input voltage with sequence input values. The fitness between the experimental and simulation results is 92.7%. The current comparison between the experimental measurement and the model simulation is shown in Figure 9. It can be observed that the identified model can predict the current correctly.

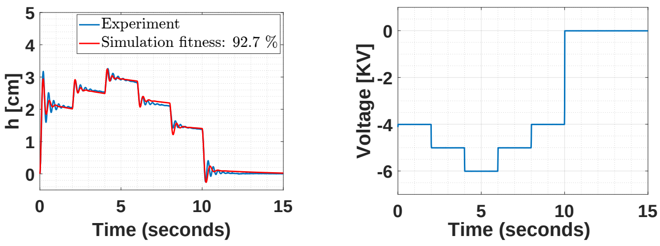

(a)

(b)

Figure 8: Model identification 8a) Comparison between model response and experimental data, 8b) Input voltage.

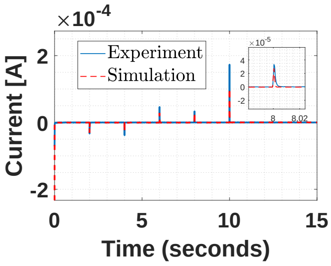

Figure 9: Current comparison between experimental and model simulation.

4.2. Parameter sensitivity

The sensitivity analysis is performed using the identified parameters: $R_2^i, C_1^i, K_b^i, b_i, \gamma_1$, and γ_2. Each parameter is varied by ±10% and ±5% from its identified value while keeping the other parameters fixed. The standard deviation (SD) of the fitness values is obtained using the MATLAB function *std* for each parameter. A higher SD indicates that variations in the corresponding parameter have a greater impact on the system's response. The results are summarized in Table 5.

Table 5: Sensitivity of key model parameters

Identified parameters	Fitness +10%	 +5%	 0%	 -5%	 -10 %	Standard Deviation
R_2^i	92.14 %	92.58 %	92.7 %	92.46 %	91.65 %	0.4219
C_1^i	92.28 %	92.6 %	92.7 %	92.57 %	92.09 %	0.2539
K_b^i	90.33 %	92.04 %	92.7 %	92.06 %	90.34 %	1.0908
b_i	92.61 %	92.67 %	92.7 %	92.7 %	92.66 %	0.0370
γ_1	81.29 %	88.35 %	92.7 %	86.7 %	75.15 %	6.7834
γ_2	89.27 %	91.68 %	92.7 %	91.82 %	89.52 %	1.5172

The most sensitive parameters are the gains in the input map. Furthermore, variations in system stiffness result in a notably high standard deviation, indicating a significant influence on the system response.

4.3. Model validation

To validate the model, we use two different experimental datasets. Dataset # 1 (Figure 10) considers successive negative input steps of 500 V every 2 seconds from 2 to 10 seconds. Subsequently, we compare the simulation results with experimental data from Dataset # 2 (see Figure 11) where a positive signal was applied. The fitness between the model and experimental data were computed using the fitting values, representing the norm of the error with the normalized mean squared root error (NRMSE) as a cost function.

$$fit(i) = \frac{\| x_{ref}(:) - x_{data}(:) \|}{\| x_{ref}(:) - mean(x_{ref}(:)) \|} \tag{23}$$

where $\| \, . \, \|$ is the 2-norm of the vector. Thus, the model fitness is computed using the MATLAB function *goodnessOfFit* with the cost function NRMSE.

In the aforementioned scenarios, the fitness ratios were 83.1% and 91.27%, illustrating good agreement between the model and the experiments. A variation of 10% in the parameters was considered to illustrate the behavior of the actuator with similar characteristics. The difference in the model response when varying the values of the sensitive parameters by ± 10% increases over time due to the effect of drift. The significant impact of the drift effect on the model response is evident.

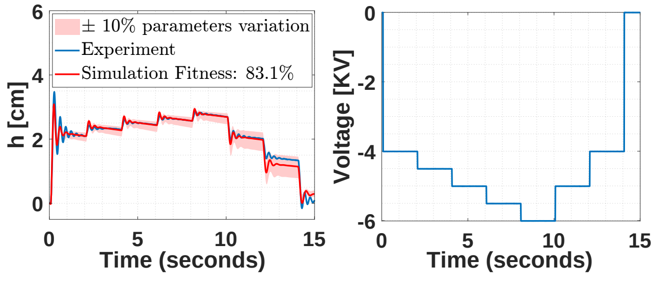

(a)

(b)

Figure 10: Model Validation Dataset # 1 10a) Comparison between model response and experimental Dataset #1, 10b) Input voltage.

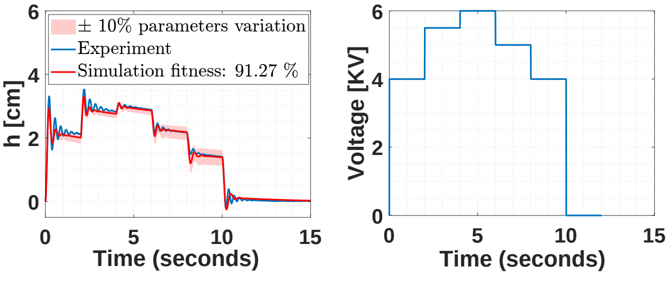

(a)

(b)

Figure 11: Model Validation, 11a) Comparison between model response and experimental Dataset # 2. 11b) Input voltage Dataset # 2.

By varying conductance $\bar{R}_0$, the current peaks of the identified model response fit correctly with the experimental results, as shown in Figure 12a and 12b.

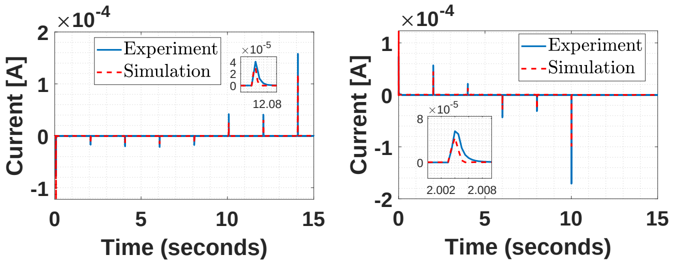

(a)

(b)

Figure 12: Model current validation, comparison between model current response and experimental 12a) Dataset # 1. 12b) Dataset # 2.

4.4. Model validation for AC input signal

The AC voltage input can effectively mitigate the drift effect of the HASEL actuator induced by the charge retention. In this section, we demonstrate that the proposed model can also represent the dynamic response of the HASEL to an AC input voltage. To validate the model, we apply a 5 kV AC signal with a 4 Hz frequency and a duty cycle of 50% and the same signal with a 2 Hz frequency in 13, 16 respectively; the corresponding parameters are detailed in 4. The fitness ratios are 85.11% and 81.03% respectively. 14, 17 present the model's response alongside the experimental data over a longer period. 15, 18 illustrate the comparison of the current. These results indicate a strong correlation between the simulated model and the experimental data under the specified AC input conditions.

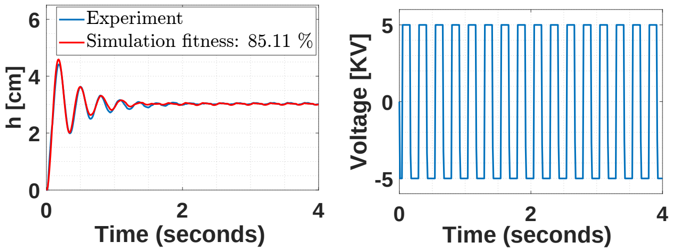

(a)

(b)

Figure 13: Model validation 13a) Comparison between model response and experimental dataset with a 4 Hz AC input signal,13b) Input signal.

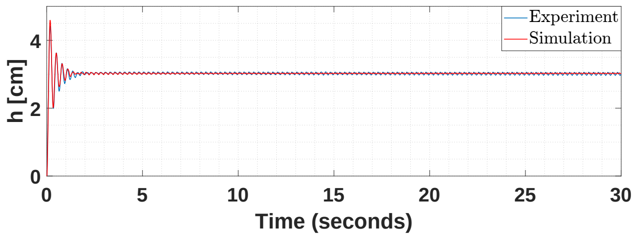

Figure 14: Model simulation in 30 s.

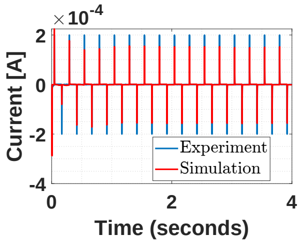

Figure 15: Comparison between current model response and experimental current.

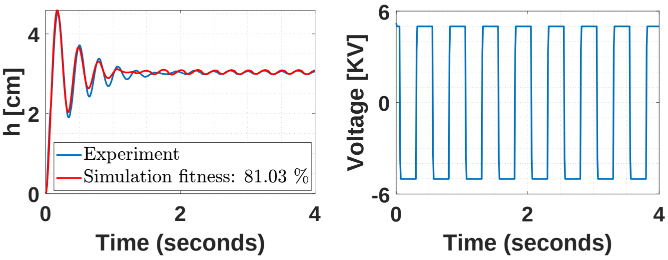

(a)

(b)

Figure 16: Model Validation 16a) Comparison between model response and experimental data with a 2Hz AC input signal, 16b) Input signal.

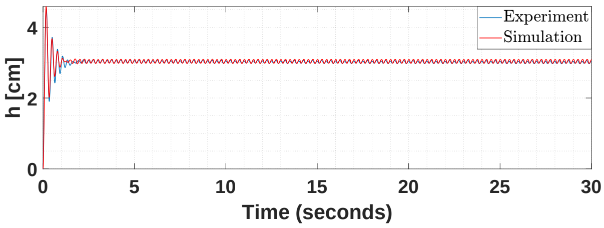

Figure 17: Model validation in 30 s.

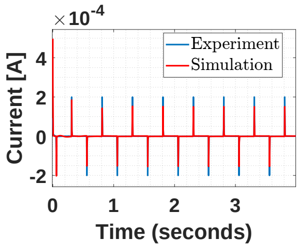

Figure 18: Current comparison.

4.5. Bio-inspired robotics application

This section presents the model of a bio-inspired Manta Ray HASEL robot following the methodology introduced in Section 3. The model was identified and validated in the same way as in Section 4.

The objective is to replicate the flapping of the Manta Ray fins. To achieve this, we used a HASEL actuator with bending motion for each fin. The strain-limiting layer, made of a polymer, enables the bending motion and defines the shape of the Manta Ray. The model of the bio-inspired HASEL robot has the same structure as the curling HASEL model (21), with the difference being that the electrodes are only on one side of the actuator, so the dimension of each state in the electrical part is 1. The HASEL actuator is composed by a single pouch with a corrugated shape. Each corrugated part can be seen as a individual shell that shares the liquid with the other shells and the unique chamber. The model is equivalent to the interconnection of two types of basic systems: one corresponding to the chamber and the others representing the interconnection of multiple shells. This is achieved thanks to the modularity property of the model. The schematic representation of the model is shown in Figure 19, while the CAD design of the Manta Ray robot is depicted in Figure 20. The black component represents the electrode, whereas the transparent section corresponds to the curling HASEL actuator, which enables the bending motion.

Figure 21 illustrates the real-life Manta Ray robot in our laboratory (Figure 21a) along with its motion. Specifically, Figure 21b depicts the robot's state without an applied voltage, while Figure 21c demonstrates its deformation under an applied voltage of 5 kV.

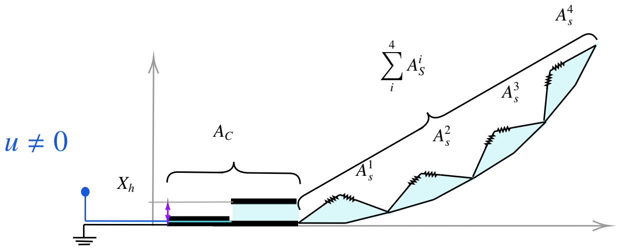

Figure 19: Manta Ray fin schematic representation.

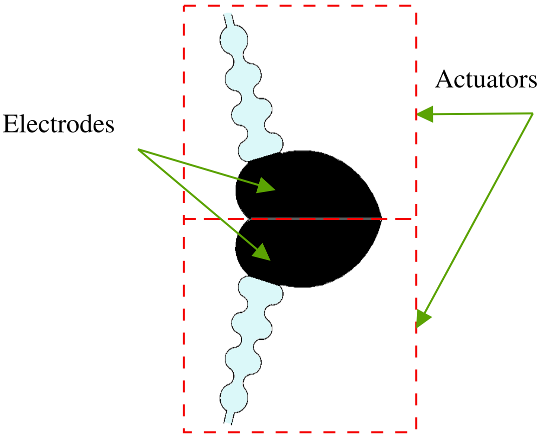

Figure 20: Manta Ray CAD design.

We define the next geometric relations, considering that the total area (A_T) is equal to the sum of the pouches plus the area of the single chamber A_c.

$$A_T = \sum_{i=1}^{n} A_s^i + A_c \tag{24}$$

The zipped length is computed considering the total area and the sum of the shell areas:

$$l_e = L_e - \frac{1}{X_h}(A_T - \sum_{i=1}^{n} A_s^i) \tag{25}$$

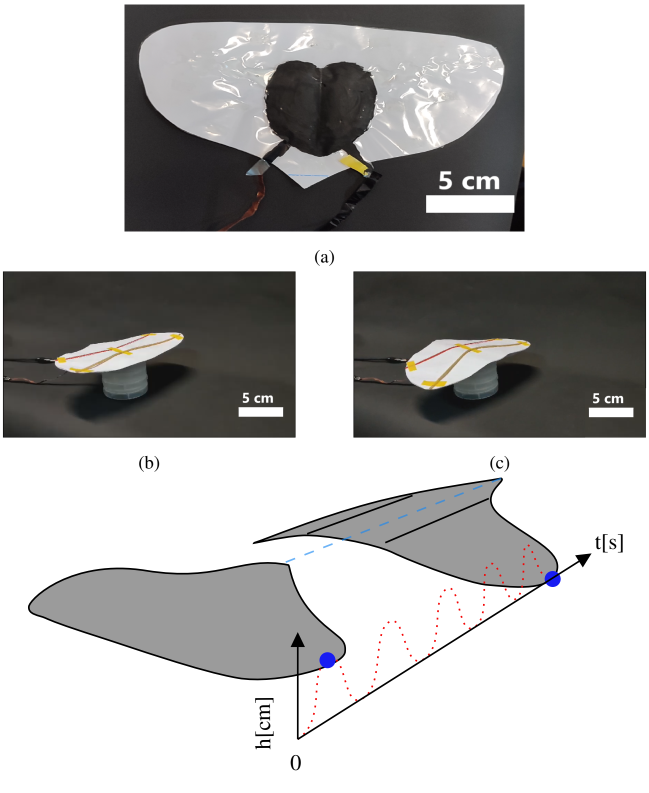

(a)

(b)

(c)

(d)

Figure 21: Manta Ray bio-inspired HASEL. 21a) Manta Ray bottom view. 21b), and 21c), Manta Ray movement. [FEMTO-ST]. 21d) Representation of the Manta Ray movement along the time.

where L_e is the electrodes length, X_h is the high of the chamber when the electrodes are unzipped. The displacement of the endpoint is:

$$h(\theta) = L_v\left(\sum_{j=1}^{n} \sin\left(\sum_{i=1}^{j} \theta_i\right)\right) \tag{26}$$

where L_v is the bottom layer length.

The energy expressions are the same than in Section 3. The equivalent electric circuit model considered for the bio-inspired HASEL robot is shown in Figure 4.

The capacitance C_2 is a function of the angle θ_i and the top film length l_p^i, it is equal to:

$$C_2(\theta_i, l_p^i) = \epsilon_0 \epsilon_r w \left(\frac{l_e(\theta_i, l_p^i)}{2t} + \frac{L_e - l_e(\theta_i, l_p^i)}{2t + X_h}\right) \tag{27}$$

where ϵ_0 is the vacuum permittivity, ϵ_r is the relative permittivity, w is the actuator width, t is the film thickness.

4.6. Model identification and validation

The input signals used for the identification and validation are sinusoidal because the aim is to represent the periodic movement of the Manta Ray (see Figure 21d). The model parameters were identified with 5 [kV] and 1 [Hz] sinusoidal input signal (see Table 6). The fitness of the identification is 80.11 % (see Figure 22). The validation was done with a 5 [kV] and 0.5 [Hz] sinusoidal input signal with a fitness of 77 % (see Figure 23). The fitness for both identification and validation is lower than the values obtained for the curling HASEL model. This can be explained by the more complex shape of the actuator. Nevertheless, it is observed that the model represents the behavior of the bio-inspired robot quite well. The reader is referred to the video, which illustrates the behavior of both the curling actuator and the Manta Ray HASEL robot.

Table 6: Bio-inspired robot model parameters

Symbol	Value	Units	Definition
L_p	0.015	m	Initial length of top film
L_v	0.015	m	Length of bottom film
L_e	0.05	m	Length of electrodes
X_h	0.002	m	Chamber high
m	0.018	kg	Total mass
ϵ_r	2.2	F/m	Relative permittivity
ϵ_0	8.854x10^{-12}	F/m	Vacuum permittivity
w	0.05	m	Actuator width
t	18×10^{-6}	m	Film thickness
R_0^i	1×10^3	Ω	Equivalent resistance
R_1^i	1.18×10^5	Ω	Equivalent resistance
R_2^i	1.55×10^6	Ω	Equivalent resistance
C_1^i	2.05×10^{-5}	C	Capacitance related to drift effect
K_i	0.7	N/m	Spring constant
K_b^i	0.2616	Nm/rad	Torsional spring constant
b_i	0.0266	kgs	Damping
γ_1	42	-	Gain parameter
γ_2	8.9	-	Gain parameter

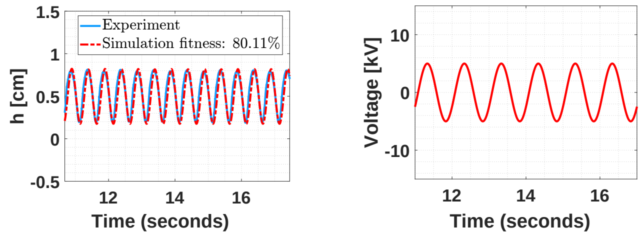

(a)

(b)

Figure 22: Identification result. 22a) Comparison between model response and experimental Manta Ray bio-inspired HASEL fin's movement data with a 1Hz AC input signal, 22b) Input signal.

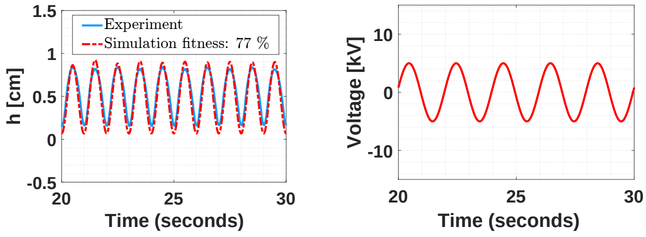

(a)

(b)

Figure 23: Validation result. 23a) Fin movement. Comparison between model response and experimental data with a 0.5Hz AC input signal, 23b) Input signal.

Discussion: The curling HASEL actuator exhibits complex non-linear behavior, and the presence of drift poses challenges in developing a model that accurately captures both its dynamic and static responses. Nevertheless, the identified model provides a response that closely aligns with the experimental data, even though it does not perfectly match the real actuator's pouch configuration in terms of number and dimensions. The primary goal of this model is to enable effective control of the HASEL actuator. By adopting a PHS approach, the derivation of non linear controllers becomes more accessible, which are available in the literature for other soft actuators [22, 23, 24, 25]. The drift effect is a slow dynamics that has to be taken into account during control design. It is the case when applying energy based techniques such as IDA-PBC technique using the model that includes the drift effect. An alternative to eliminate drift is the application of an AC signal, which discharges the actuator and prevents the accumulation of an internal electric field. The drawbacks of this method are that it requires a voltage source capable of generating this type of signal and there is a ripple in the actuator's response.

5. Conclusions

We employ the PH approach to model a curling HASEL actuator by dividing its dynamics into two distinct components. The mechanical aspect is characterized by linear and torsional springs coupled with a mass, whereas the electrical component consists of a varying capacitor C_2^i in parallel with resistance R_2^i, both in series with capacitor C_1^i in parallel with a resistance R_1^i. This model effectively captures both the drift phenomenon and the intricate dynamics of the actuator. Moreover, the proposed PH system model demonstrates robustness in representing system dynamics across a range of input voltage values, regardless of polarity. Once calibrated, the model allows for the adjustment of the resistance R_0^i value to fine-tune the total measured current, providing flexibility in matching experimental observations. Furthermore, the model proved adept at simulating the response of the actuator to an AC signal, effectively mitigating the drift effect induced by charge retention. This capability enhances its utility in practical applications where the stability and accuracy of actuation are crucial. The use of the port-Hamiltonian (PH) framework for modeling the dynamics of the HASEL actuator offers two main advantages. First, the modularity of the port-Hamiltonian system (PHS) model facilitates the interconnection of different components of the actuator, such as the mechanical and electrical subsystems. This modular structure also enables seamless integration with other systems, for example, the bio-inspired Manta Ray robot presented in the paper and a flexible structure actuated by the HASEL actuator. Second, the PH framework is well-suited for control design using passivity-based methods, such as the Interconnection and Damping Assignment Passivity-Based Control (IDA-PBC) approach.

In future work, the model can be extended to an infinite-dimensional model to capture the actuator compliance deformation more precisely. For example, the proposed model can be integrated with a beam model to represent more complex systems composed of mechanisms and HASEL actuators. This advancement would provide a more detailed representation of the actuator behavior under varying conditions. Additionally, the proposed model holds promise for the design and implementation of various nonlinear control strategies. These advanced control techniques leverage the fidelity of the model to achieve robust and precise control over actuator dynamics. Such approaches are particularly beneficial for high-performance and stable applications where conventional linear control methods may fall short. The potential application of the proposed model in self-sensing for HASEL actuators will be explored, inspired by the approach presented in [26].

Acknowledgement

This work is supported by the EIPHI Graduate School (contract ANR-17-EURE-0002) and Région Franche-Comté. This work has been partly supported by the French ROBOTEX network (TIRREX ANR-21-ESRE-0015) and its FEMTO-ST technological facility CMNR. The second and fourth authors thank the European Marie Skłodowska-Curie Actions Project MODCONFLEX (Grant No. 101073558) for its support.

Conflict of Interest declaration

The authors declare that they have NO affiliations with or involvement in any organization or entity with any financial interest in the subject matter or materials discussed in this manuscript.

References

[1] E. Acome, S. K. Mitchell, T. Morrissey, M. Emmett, C. Benjamin, M. King, M. Radakovitz, C. Keplinger, Hydraulically amplified self-healing electrostatic actuators with muscle-like performance, Science 359 (6371) (2018) 61–65.

[2] P. Rothemund, N. Kellaris, S. K. Mitchell, E. Acome, C. Keplinger, Hasel artificial muscles for a new generation of lifelike robots—recent progress and future opportunities, Advanced materials 33 (19) (2021) 2003375.

[3] S. Kim, Y. Cha, Double-layered electrohydraulic actuator for bidirectional bending motion of soft gripper, in: 2021 18th International Conference on Ubiquitous Robots (UR), IEEE, 2021, pp. 645–649.

[4] K. Ly, J. V. Mayekar, S. Aguasvivas, C. Keplinger, M. E. Rentschler, N. Correll, Electro-hydraulic rolling soft wheel: Design, hybrid dynamic modeling, and model predictive control, IEEE Transactions on Robotics 38 (5) (2022) 3044–3063.

[5] Y. Tian, J. Liu, W. Wu, X. Liang, M. Pan, C. Bowen, Y. Jiang, J. Sun, T. McNally, D. Wu, et al., Peano-hydraulically amplified self-healing electrostatic actuators based on a novel bilayer polymer shell for enhanced strain, load, and rotary motion, Advanced Intelligent Systems 4 (5) (2022) 2100239.

[6] N. Kellaris, P. Rothemund, Y. Zeng, S. K. Mitchell, G. M. Smith, K. Jayaram, C. Keplinger, Spider-inspired electrohydraulic actuators for fast, soft-actuated joints, Advanced Science 8 (14) (2021) 2100916.

[7] Z. Yoder, D. Macari, G. Kleinwaks, I. Schmidt, E. Acome, C. Keplinger, A soft, fast and versatile electrohydraulic gripper with capacitive object size detection, Advanced Functional Materials 33 (3) (2023) 2209080.

[8] C. A. Manion, D. K. Patel, M. Fuge, S. Bergbrieter, Modeling and evaluation of additive manufactured hasel actuators, in: International Conference on Intelligent Robots and Systems (IEEE/RSJ), 2018.

[9] N. Kellaris, V. G. Venkata, P. Rothemund, C. Keplinger, An analytical model for the design of peano-hasel actuators with drastically improved performance, Extreme Mechanics Letters 29 (2019) 100449.

[10] X. Wang, S. K. Mitchell, E. H. Rumley, P. Rothemund, C. Keplinger, High-strain peano-hasel actuators, Advanced Functional Materials 30 (7) (2020) 1908821.

[11] P. Rothemund, S. Kirkman, C. Keplinger, Dynamics of electrohydraulic soft actuators, Proceedings of the National Academy of Sciences 117 (28) (2020) 16207–16213.

[12] A. Volchko, S. K. Mitchell, T. G. Morrissey, J. S. Humbert, Model-based data-driven system identification and controller synthesis framework for precise control of siso and miso hasel-powered robotic systems, in: 2022 IEEE 5th International Conference on Soft Robotics (RoboSoft), IEEE, 2022, pp. 209–216.

[13] T. Hainsworth, I. Schmidt, V. Sundaram, G. L. Whiting, C. Keplinger, R. MacCurdy, Simulating electrohydraulic soft actuator assemblies via reduced order modeling, in: 2022 IEEE 5th International Conference on Soft Robotics (RoboSoft), IEEE, 2022, pp. 21–28.

[14] A. Washington, Z. Olsen, J. Su, K. J. Kim, A physics-based modeling of a hydraulically amplified electrostatic actuator, Journal of Physics Communications 6 (8) (2022) 085007.

[15] Z. Chen, F. Renda, A. Le Gall, L. Mocellin, M. Bernabei, T. Dangel, G. Ciuti, M. Cianchetti, C. Stefanini, Data-driven methods applied to soft robot modeling and control: A review, IEEE Transactions on Automation Science and Engineering (2024).

[16] Y. Yeh, N. Cisneros, Y. Wu, K. Rabenorosoa, Y. Le Gorrec, Modeling and position control of the hasel actuator via port-hamiltonian approach, IEEE Robotics and Automation Letters 7 (3) (2022) 7100–7107.

[17] G. Flores, M. W. Spong, The soft-pvtol: modeling and control, Robotics and Autonomous Systems (2025) 104925.

[18] Z. Liu, H. McAleese, A. Weightman, G. Cooper, Optimization of hydraulically amplified electrostatic actuators based on an evolutionary strategy and finite element model to match the performance of the human triceps surae muscle fibres, Extreme Mechanics Letters 63 (2023) 102050.

[19] I.-D. Sîrbu, D. Preninger, D. Danninger, L. Penkner, R. Schwödiauer, G. Moretti, N. Arnold, M. Fontana, M. Kaltenbrunner, Electrostatic actuators with constant force at low power loss using matched dielectrics, Nature Electronics 6 (11) (2023) 888–899.

[20] E. Rumley, P. Rothemund, S. Zhang, N. Kellaris, C. Keplinger, Characterization of charge retention effects in hasel actuators, in: Electroactive Polymer Actuators and Devices (EAPAD) XXIV, SPIE, 2022, p. PC120420B.

[21] A. Van der Schaft, L2-Gain and Passivity Techniques in Nonlinear Control, Lecture Notes in Control and Information Sciences, Springer, 2000.

[22] E. Franco, A. Garriga-Casanovas, J. Tang, F. R. y Baena, A. Astolfi, Adaptive energy shaping control of a class of nonlinear soft continuum manipulators, IEEE/ASME Transactions on Mechatronics 27 (1) (2021) 280–291.

[23] E. Franco, A. G. Casanovas, J. Tang, F. R. y Baena, A. Astolfi, Position regulation in cartesian space of a class of inextensible soft continuum manipulators with pneumatic actuation, Mechatronics 76 (2021) 102573.

[24] A. Mattioni, Y. Wu, H. Ramirez, Y. Le Gorrec, A. Macchelli, Modelling and control of an ipmc actuated flexible structure: A lumped port hamiltonian approach, Control Engineering Practice 101 (2020) 104498.

[25] W. Zhou, Y. Wu, H. Hu, Y. Li, Y. Wang, Port-hamiltonian modeling and ida-pbc control of an ipmc-actuated flexible beam, in: Actuators, Vol. 10, MDPI, 2021, p. 236.

[26] C. Silva-Plata, C. Rosel, B. G. Cangan, H. Alagi, B. Hein, R. K. Katzschmann, R. Fernández, Y. Mojtahedi, S. E. Navarro, Model-based capacitive touch sensing in soft robotics: Achieving robust tactile interactions for artistic applications, IEEE Robotics and Automation Letters 10 (5) (2025) 4596–4603.

Nelson Cisneros received the degree of MSc. in Engineering Sciences with a mention in Electrical Engineering at the Universidad de Concepción, Chile. He is currently third year Ph.D. student in AS2M department of FEMTO-ST institute, Besançon, France. His research field is soft robotics actuators with port-Hamiltonian (PH) framework.

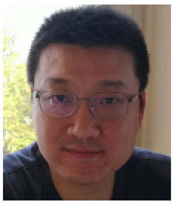

Yongxin Wu received his engineer degree in Transportation Information and Control from the University of Chang'an, Xi'an, China in 2010 and his Master's degree in Automatic Control from the University Claude Bernard of Lyon, Villeurbanne, France in 2012. He received his Ph.D. degree in Automatic Control in 2015 at the University Claude Bernard of Lyon, Villeurbanne, France. From 2015 to 2016, He held a postdoctoral and teaching assistant position at LAGEP. Since 2016, he has been an Associate Professor of Automatic Control at Université Marie et Louis Pasteur, SUPMICROTECH-ENSMM, and affiliated to the AS2M department at FEMTO-ST institute (UMR CNRS 6174) in Besançon, France. He is an IEEE Senior Member actively involved in IEEE CSS TC on Distributed Parameter systems, IFAC TC 2.6 on Distributed Parameter systems and TC 4.2 on Mechatronic Systems. He is also a member of the IEEE CSS Technology Conference Editorial Board (TCEB). His research interests include port Hamiltonian systems, model and controller reduction, modelling and control of multi-physical systems, particularly soft actuators based on the electro-active polymers.

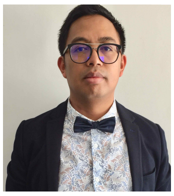

Kanty Rabenorosoa received the M.S. degree in electrical engineering from Institut National des Sciences Appliquées Strasbourg, Strasbourg, France, in 2007, and the Ph.D. degree in automatic control from the University of Franche-Comté, Besançon, France, in 2010. He was a Post-Doctoral Fellow at Laboratoire d'Informatique, de Robotique et de Micro-électronique de Montpellier, University of Montpellier, France, from 2011 to 2012. He was an associate professor at the Engineering school SupMicroTech-ENSMM from 2012 to 2023. He is currently a full Professor at Université Marie et Louis Pasteur (uMLP), AS2M Department, FEMTO-ST Institute, Besançon. His research interests include mechatronics, smart actuator, soft and continuum microrobotics for medical applications within the RoMoCo team.

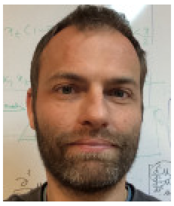

Yann Le Gorrec was graduated as engineer in “Control, Electronics, Computer Engineering” at the National Institute of Applied Sciences (INSA, Toulouse, France) in 1995. He received in 1998 his Ph. D. degree from the National Higher School of Aeronautics and Aerospace (Supaero, Toulouse, France). His field of interest was robust control and self-scheduled controller synthesis. From 1999 to 2008, he was Associate Professor in Automatic Control at the Laboratory of Control and Chemical Engineering of Lyon Claude Bernard University (LAGEP, Villeurbanne, France). He worked on port Hamiltonian systems and their use for the modelling and control of irreversible and distributed parameter systems with an application to physic-chemical processes. Since September 2008 he is full Professor at National Engineering Institute in Mechanics and Microtechnologies of Besançon, France. His current field of research is the control of nonlinear and distributed parameter systems with an application to smart material-based actuators and micro systems by using the port Hamiltonian framework.